Inorganic Chemistry

Article

pubs.acs.org/IC

New Water Oxidation Chemistry of a Seven-Coordinate Ruthenium Complex with a Tetradentate Polypyridyl Ligand

James T. Muckerman,*[,†] Marta Kowalczyk,*[,†] Yosra M. Badiei,[†] Dmitry E. Polyansky,[†] Javier J. Concepcion,[†] Ruifa Zong,[‡] Randolph P. Thummel,[‡] and Etsuko Fujita[†]

[†]Chemistry Department, Brookhaven National Laboratory, Upton, New York 11973-5000, United States

[‡]Department of Chemistry, University of Houston, Houston, Texas 77204-5003, United States

Supporting Information

ABSTRACT: The mononuclear ruthenium(II) complex $[\mathbf{Ru}]^{2+}$ (**Ru** = Ru(dpp)(pic)$_2$, where dpp is the tetradentate 2,9-dipyrid-2′-yl-1,10-phenanthroline ligand and pic is 4-picoline) reported by Thummel's group (*Inorg. Chem.* **2008**, 47, 1835−1848) that contains no water molecule in its primary coordination shell is evaluated as a catalyst for water oxidation in artificial photosynthesis. A detailed theoretical characterization of the energetics, thermochemistry, and spectroscopic properties of intermediates allowed us to interpret new electrochemical and spectroscopic experimental data, and propose a mechanism for the water oxidation process that involves an unprecedented sequence of seven-coordinate ruthenium complexes as intermediates. This analysis provides insights into a mechanism that generates four electrons and four protons in the solution and a gas-phase oxygen molecule at different pH values. On the basis of the calculations and corroborated substantially by experiments, the catalytic cycle goes through $[^2\mathbf{Ru}^{III}]^{3+}$ and $[^2\mathbf{Ru}^{V}(O)]^{3+}$ to $[^1\mathbf{Ru}^{IV}(OOH)]^{3+}$ then $[^2\mathbf{Ru}^{III}(\cdots{}^3O_2)]^{3+}$ at pH 0, and through $[^3\mathbf{Ru}^{IV}(O)]^{2+}$, $[^2\mathbf{Ru}^{V}(O)]^{3+}$, and $[^1\mathbf{Ru}^{IV}(OO)]^{2+}$ at pH 9 before reaching the same $[^2\mathbf{Ru}^{III}(\cdots{}^3O_2)]^{3+}$ species, from which the liberation of the weakly bound O_2 might require an additional oxidation to form $[^3\mathbf{Ru}^{IV}(O)]^{2+}$ to initiate further cycles involving all seven-coordinate species.

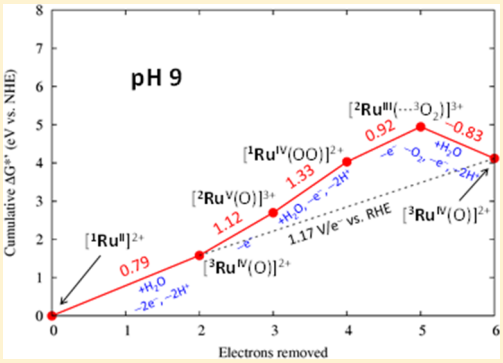

INTRODUCTION

Water oxidation ($2H_2O \rightarrow 4H^+ + 4e^- + O_2$) is an energetically demanding and critical half-reaction that is essential for the development of clean and sustainable fuel technologies.[1−6] The photosynthetic oxygen-evolving complex (OEC) in Photosystem II can oxidize water to oxygen at a potential near the thermodynamic limit (1.23 V vs NHE at pH 0) by taking advantage of energetically favorable proton-coupled electron transfer (PCET) pathways.[7−11] Thus, it is important to develop new water-oxidation catalysts (WOC) that can efficiently mediate the four consecutive PCET steps and thereby minimize undesirable overpotentials.[12]

The quest for such catalysts has been advanced in recent years by the successful integration of theoretical/computational studies with experiment.[13−30] Our previous theoretical and experimental studies of water oxidation by a mononuclear ruthenium polypyridyl catalyst, $[\mathbf{Ru}^{II}(OH_2)]^{2+}$, (**Ru** = Ru^{II}(NPM)(pic)$_2$, NPM = 4-*t*-butyl-2,6-di(1′,8′-naphthyrid-2′-yl)-pyridine and pic =4-picoline), that contains an aqua ligand in an equatorial position and has appropriately positioned π^* orbitals in the tridentate NPM ligand for promoting an initial $2e^-/2H^+$ oxidation step,[18] demonstrated that this catalyst exhibits the remarkable feature of promoting formation of an O−O bond through the direct proton-coupled electron-transfer (PCET) oxidation of $[\mathbf{Ru}^{IV}(O)]^{2+}$ and H_2O to form $[\mathbf{Ru}^{III}(OOH)]^{2+}$, avoiding a well-known non-PCET $Ru^V(O)$ pathway.[31] This is important because the potential of the $[\mathbf{Ru}^{IV}(O)]^{2+}/[\mathbf{Ru}^{II}(OH_2)]^{2+}$ couple decreases by 59 mV/pH as the pH increases, while that of the $[\mathbf{Ru}^{V}(O)]^{3+}/[\mathbf{Ru}^{IV}(O)]^{2+}$ couple is independent of pH. Therefore, the gap between the first of these couples and the second increases greatly with increasing pH. The reversible hydrogen electrode (RHE) moves in parallel with the $2e^-/2H^+$ $[\mathbf{Ru}^{IV}(O)]^{2+}/[\mathbf{Ru}^{II}]^{2+}$ couple with pH, so that the potential of the $[\mathbf{Ru}^{V}(O)]^{3+}/[\mathbf{Ru}^{IV}(O)]^{2+}$ couple increases with respect to the RHE with increasing pH.

In an earlier report,[32] a tentative mechanism for water oxidation based on DFT calculations was proposed for the six-coordinate Ru(II) catalyst involving the equatorial tetradentate 2,9-dipyrid-2′-yl-1,10-phenanthroline (dpp) ligand and two monodentate axial 4-picolines (pic). [The complex reported in ref 32 was the chloride salt of the same cation previously reported by Zong and Thummel[33] as the PF_6^- salt, which was not soluble in water.] This 18-electron $[\mathbf{Ru}^{II}]^{2+}$ (**Ru** = Ru(dpp)(pic)$_2$, Figure 1) complex with no aqua ligand in its primary coordination shell was predicted to accommodate a water molecule upon two-electron oxidation resulting in the seven-coordinate 18-electron $[\mathbf{Ru}^{IV}(OH_2)]$ intermediate. In this study, we have revisited the water oxidation mechanism,

Received: March 27, 2014
Published: June 9, 2014

dx.doi.org/10.1021/ic500709h | *Inorg. Chem.* 2014, 53, 6904−6913

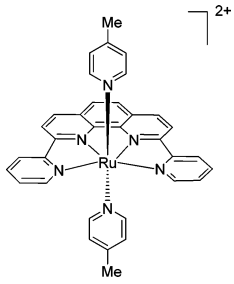

Figure 1. Structure of $[\mathbf{Ru^{II}}]^{2+}$.

and systematically investigated the properties of possible intermediates involved not only in the O−O bond formation step but also in the entire catalytic cycle. Sun and co-workers have also reported a seven-coordinate Ru(IV) dimer complex with a $[HOHOH]^-$ bridging ligand.[34]

Our present theoretical studies supported by experimental data strongly point to PCET pathways. At low pH the pathway involves a $2e^-/2H^+$ step for the formation of the seven-coordinate $[\mathbf{Ru^V}(O)]^{3+}$ species produced from the reaction of a water molecule with the one-electron oxidized $[\mathbf{Ru^{III}}]^{3+}$ species. In neutral and high pH regions, the pathway involves the $2e^-/2H^+$ PCET oxidation of $[\mathbf{Ru^{II}}]^{2+}$ and a water molecule to produce a $[\mathbf{Ru^{IV}}(O)]^{2+}$ species. These species are predicted to participate in subsequent PCET steps upon attack by another water molecule resulting in the formation of an O−O bond. Regardless of pH, spin recoupling during the formation of a "$[\mathbf{Ru^V}(OO)]^{3+}$" species results in an intermediate in which a $^3O_2$ molecule is loosely bound in an equatorial position in a seven-coordinate $[\mathbf{Ru^{III}}(\cdots{}^3O_2)]^{3+}$ intermediate that may require an additional oxidation in order to release the oxygen. These PCET events provide a convenient route, especially at moderate to high pH, for low-energy reaction pathways mediated by a sequence of plausible seven-coordinate intermediates involved in the water-oxidation catalytic cycle. Herein, we report the details of these catalytic intermediates by constructing the Pourbaix diagram, Latimer−Frost diagrams at low and high pH, and calculating the absorption spectra of these species to elucidate the mechanism of water oxidation by this catalyst. We propose a "new chemistry" for water oxidation by a mononuclear ruthenium complex that consists of an unprecedented sequence of steps involving only seven-coordinate intermediates. Because of the complicated nature of the reaction steps in the catalytic mechanism for water oxidation by the $[Ru^{II}(dpp)(pic)_2]^{2+}$ complex which involve high oxidation states of the metal center and the transfer of many protons, it is difficult to obtain a complete characterization of the mechanism from experimental studies. The present paper therefore presents the relevant structures, energetics and reaction sequences based on theoretical studies using DFT calculations, and presents key experimental results that corroborate them.

EXPERIMENTAL SECTION

Computational Details. All calculations were carried out using DFT and the B3LYP functional.[35−38] The ECP28MWB(1f,0g) effective core potential and basis[39,40] was used for the ruthenium center, and the 6-31+G(d,p) 5d basis set[41−46] was used for all other atoms. All species considered in the suggested catalytic water oxidation process were fully optimized, and frequency analyses were carried out to exclude any transition state geometries and to confirm a minimum in the energy. The CPCM solvation model[47−49] as implemented in the Gaussian 09 program package[50] was used along with UAHF radii[51] and water as solvent. TD-DFT calculations with the CPCM solvation model and the same basis set were performed for selected species to help characterize their spectral signature in the UV−vis spectra.

The standard Gibbs free energy in aqueous solution was obtained to calculate pK_a values and the standard reduction potentials to compare with experimental data and to construct theoretical Pourbaix and Latimer−Frost diagrams. The absolute free energy of each catalyst species plus appropriate "reservoir" species (electrons, protons, water molecules, oxygen molecule) in the aqueous solution (eV vs NHE) was calculated as

$$G^*_{tot} = G^*_{(aq)} + G^*_{res} \quad (1)$$

where $G^*_{(aq)} = G^\circ_{(g)} + \Delta G^{\circ\rightarrow *} + \Delta G^*_S$. Here $G^\circ_{(g)}$ is the absolute gas-phase free energy, ΔG^*_S is the (single-point) solvation free energy, and $\Delta G^{\circ\rightarrow *}$ is the change in standard state of the catalyst species from 1 atm to 1 M in the gas phase.[52] The sum of the free energies in solution (or other appropriate standard state) of all other species involved in the catalytic cycle that are not included in the catalyst species is denoted as G^*_{res} (see Supporting Information Table S1). Because of the large size and the complexity of the molecules, we will assume that there are no significant changes in the geometry obtained in the full optimization in the different phases, i.e., vacuum and aqueous solutions. As a result, we can calculate an aqueous free energy of the species as the sum of the (standard state corrected) free energy in the gas phase and the solvation free energy obtained from the difference between a single-point electronic energy calculation including the solvation model, $E_{el,S}$, and the gas-phase electronic energy, E_{el}. Within one catalytic cycle there are up to three water molecules that are required to produce O_2 (vide infra); thus the starting point for the reservoir associated with the $[^1\mathbf{Ru^{II}}]^{2+}$ species consists of three water molecules with a standard state of pure liquid water. These molecules of $H_2O_{(liq)}$ are taken from the solution (reservoir) as needed, and any electrons (standard state 1 atm in the gas phase), protons (standard state 1 M in aqueous solution), or oxygen molecule (standard state 1 atm in the gas phase) that are removed from the catalyst species during the catalytic reaction are transferred to the reservoir. The $\Delta G^{\circ\rightarrow *}$ has the value 1.894 kcal/mol and is the free energy associated with the work required to compress an ideal gas at 1 atm pressure to a molar volume of unity to make the standard states of the species the same in the gas phase and in solution. Once the relative free energies of all species and their corresponding reservoirs are obtained, they are related to the normal hydrogen electrode (NHE) by adding the appropriate multiple of $\Delta G^*(NHE) = -4.2115$ eV for the cumulative number of electrons transferred (i.e., the number of electrons in the reservoir for a given species). This value of $\Delta G^*(NHE)$ is derived from the generally accepted value of the free energy of $H^+_{(aq)}$ of −272.2 kcal/mol,[52,53] the free energy of the gas-phase electron of −0.868 kcal/mol,[54] and the calculated gas-phase absolute free energy of H_2 (−740.375 kcal/mol) with the level of theory employed here. The absolute free energy of H_2O in the pure liquid standard state is obtained from the calculated gas-phase value as $G^*_{(liq)} = G^\circ_{(g)} + \Delta G^{\circ\rightarrow *} + \Delta G^*_{self}$, where ΔG^*_{self} is the free-energy change associated with the work to take the 1 M gas at 24.465 atm pressure to the molarity and vapor pressure of the pure liquid.[55] The pK_a values are obtained from

$$pK_a = \Delta G^*_{a,(aq)}/RT\ \ln(10) \quad (2)$$

where $\Delta G^*_{a,(aq)} = G^*(A^-_{(aq)}) + G^*(H^+_{(aq)}) - G^*(HA_{(aq)})$ and represents the acid dissociation $HA_{(aq)} \rightarrow H^+_{(aq)} + A^-_{(aq)}$ at 1 M standard state in solution. The standard reduction potential (at pH 0) is defined as $E^\circ = -[G^*_{tot}(red) - G^*_{tot}(ox)]/nF$, where n is the number of electrons transferred, and $G^*_{tot}(red)$ and $G^*_{tot}(ox)$ refer to the absolute free energies of the reduced and oxidized reacting species, respectively, including their corresponding reservoirs, relative to NHE (Table 1). The pH-dependent potential was obtained from the Nernst equation

$$E = E^\circ - (m/n)0.059159pH \quad (3)$$

where m represents the number of protons transferred.

dx.doi.org/10.1021/ic500709h | Inorg. Chem. 2014, 53, 6904−6913

Table 1. Calculated Potentials and pK_a Values of the Reacting Species with the Net Numbers of Electrons and Protons Involved

species	$m(H^+)/n(e^-)$	E^o (V vs NHE) @ pH 0 (pH 9)[a]
$[^2Ru^{III}]^{3+}/[^1Ru^{II}]^{2+}$	$1e^-$	0.82 (0.82)
$[^3Ru^{IV}(O)]^{2+}/[^1Ru^{II}]^{2+}$	$2H^+/2e^-$	1.32 (0.79)
$[^3Ru^{IV}(O)]^{2+}/[^2Ru^{III}]^{3+}$	$2H^+/1e^-$	1.83 (0.76)
$[^1Ru^{IV}(OH)]^{3+}/[^2Ru^{III}]^{3+}$	$1H^+/1e^-$	1.61 (1.07)
$[^2Ru^{V}(O)]^{3+}/[^2Ru^{III}]^{3+}$	$2H^+/2e^-$	1.47 (0.94)
$[^2Ru^{III}(OOH)]^{2+}/[^3Ru^{IV}(O)]^{2+}$	$1H^+/1e^-$	1.68 (1.15)
$[^1Ru^{IV}(OO)]^{2+}/[^2Ru^{III}(OOH)]^{2+}$	$1H^+/1e^-$	1.83 (1.30)
$[^2Ru^{III}(\cdots{}^3O_2)]^{3+}/[^1Ru^{IV}(OO)]^{2+}$	$1e^-$	0.92 (0.92)
$[^2Ru^{V}(O)]^{3+}/[^3Ru^{IV}(O)]^{2+}$	$1e^-$	1.12 (1.12)
$[^1Ru^{IV}(OOH)]^{3+}/[^2Ru^{V}(O)]^{3+}$	$1H^+/1e^-$	1.96 (1.43)
$[^2Ru^{III}(\cdots{}^3O_2)]^{3+}/[^1Ru^{IV}(OOH)]^{3+}$	$1H^+/1e^-$	1.35 (0.82)
$[^3Ru^{IV}(O)]^{2+}/[^2Ru^{III}(\cdots{}^3O_2)]^{3+}$	$2H^+/1e^-$	0.24 (−0.83)
$[^1Ru^{IV}(OOH)]^{3+}/[^2Ru^{III}(OOH)]^{2+}$	$1e^-$	1.40 (1.40)
$[^1Ru^{IV}(OO)]^{2+}/[^2Ru^{V}(O)]^{3+}$	$2H^+/1e^-$	2.40 (1.33)
$[^1Ru^{IV}(OOH)]^{3+}/[^1Ru^{IV}(OO)]^{2+}$	pK_a	7.34
$[^3Ru^{IV}(O)]^{2+}/[^2Ru^{III}(OH)]^{2+}$	$1H^+/1e^-$	1.17 (0.64)
$[^1Ru^{IV}(OO)]^{2+}/[^1Ru^{IV}(OH)]^{2+}$	$2H^+/2e^-$	1.87 (0.80)

[a]For example, the potential for the $[^3Ru^{IV}(O)]^{2+}/[^2Ru^{III}]^{3+}$ couple has the value $E = 1.827-0.1183 \times 9 = 0.762$ V vs NHE at pH 9 by eq 3.

Electrochemical Measurements. Electrochemical measurements were conducted with a BAS 100b potentiostat from Bioanalytical Systems. All potentials in aqueous solutions are reported vs NHE. Cyclic voltammograms (CV) and square-wave voltammograms (SWV) were performed at various pH for $[\mathbf{Ru^{II}}]^{2+}$ (1 mM) and were recorded using single component buffers (phosphate, acetate or carbonate solutions) with ionic strength μ = 0.1 M. Between pH 1.5 and 8, a 0.1 M aqueous phosphate buffer (NaH_2PO_4) was used, and the pH of the solution was adjusted by using 0.1 M $HClO_4$ or NaOH. For pH 5 to 6, a 0.1 M acetate/acetic acid buffer was prepared. Measurements at pH 1 were performed in 0.1 M $HClO_4$ and at basic pH (9−10) were carried out in a 0.1 M carbonate−bicarbonate buffer. A glassy carbon disk or boron-doped diamond was used as the working electrode, a platinum wire as a counter electrode, and Ag/AgCl (sat. KCl) as a reference electrode fitted in a one-compartment cell. Bulk electrolysis (BE) was performed using a Pt mesh as a working electrode and the Pt counter electrode was isolated using a double junction. Counter and reference electrodes were placed in a separate double junction compartment. An aqueous solution of ∼1 mM of $[\mathbf{Ru^{II}}]^{2+}$ in 0.1 M H_2SO_4 was prepared at pH 1, and in 50 mM phosphate buffer at pH 6 or 7, respectively. At pH 1 an applied potential of 1350 mV vs NHE was held constant throughout the experiment, and at pH 6 or 7, a constant potential of 1050 mV or 1400 mV vs NHE was applied. UV−vis spectroscopy using a 2 mm cell confirmed the consumption of the starting material and the formation of the oxidation products.

Analytical Measurements. Electronic absorption spectra were recorded with a UV−visible Agilent 8453 diode-array or a Hewlett-Packard (HP) spectrophotometer and were corrected for the background spectrum of the solvent. Electrospray ionization mass spectra (ESI-MS) were acquired with a Thermo Finnigan mass spectrometer. ^1H and ^{13}C NMR spectra were recorded at room temperature using a Bruker Avance spectrometer operating at 400 MHz for ^1H. Chemical shifts are reported in parts per million (ppm) referenced to the residual solvent peak for ^1H. The pH values were measured using a Fisher Scientific accumet Microglass electrode after calibration with standard buffer solutions. Oxygen measurements were performed using an Ocean Optics HIOXY fluorescent oxygen probe with a factory provided multipoint calibration. A single point reset was performed for each catalytic run. A three neck round-bottom flask with two side arms equipped with T bore Teflon plugs was used to purge the flask and the inlet was used for oxidant injection and the third neck was modified to accommodate the O_2 probe. The total working volume was 34 mL. The gastight vessel containing the ruthenium complex $[\mathbf{Ru^{II}}]^{2+}$ (0.18 mM) catalyst in 4 mL of water was equipped with a stir bar and placed in a temperature controlled water bath (19 °C). The solution was purged with Argon and an aliquot of 200 equiv of Ce(IV) (36 mM, 4 mL, 0.1 M $HClO_4$) was added. The vessel was sealed and the time evolution of the partial pressure of O_2 in the head space was recorded using Ocean Optics Neofox software. Resonance Raman (RR) spectra were recorded using a home-built spectrometer equipped with a SpectraPro 300i spectrograph (Acton) and a liquid nitrogen cooled Spec-10 CCD (Acton). The output of an Innova 70C-Spectrum Ar/Kr ion laser (457.9 nm, 30 mW) was used as the excitation source). A corresponding laser line and long pass filters (Semrock) were used before and after the sample, respectively. Aqueous solutions of metal complexes (∼1 mM) were frozen inside an EPR tube and placed into an EPR quartz dewar (H. S. Martin). All RR measurements were performed at 77 K using 30 min averaging.

RESULTS

Structural Identity of $[Ru^{II}]^{2+}$ in Aqueous Solution. The crystal structure of $[\mathbf{Ru^{II}}]^{2+}$ was reported previously.[32] The complex exhibits C_{2v} symmetry and has a wide bite angle of 125.6° for coordination of two pyridyl functional groups of the dpp ligand. The coordination geometry is retained in aqueous solutions as evidenced by ESI-MS and NMR spectra (Supporting Information Figures S1 and S2). No axial ligand loss was observed even in acidic aqueous solution, in which the protonated form of free picoline is expected to coordinate less strongly compared to its conjugate base. Also, no symmetry loss was observed for dpp coordination in D_2O, indicating that the pyridyl groups of dpp are not in equilibrium between the free and coordinated state. Our calculated geometry of $[^1\mathbf{Ru^{II}}]^{2+}$ at the DFT/B3LYP level of theory agrees with the available crystallographic structure of $[\mathbf{Ru^{II}}]^{2+}$ previously reported by Thummel (see Supporting Information Table S2).[32] Calculated bond lengths, angles and dihedral angle of the dpp ligand are in very good agreement with the experimental data. The detailed information about the bond lengths and bond angles, including the dihedral angles of the tetradentate dpp ligand, are listed in the Supporting Information. Our theoretical studies also included an investigation of the possibility of an axial picoline ligand being replaced by a solvent water molecule. The standard free energy of $[\mathbf{Ru^{II}}]^{2+} + H_2O_{(liq)}$ is calculated to be 18.02 kcal/mol lower than that of $[Ru^{II}(dpp)(pic)(H_2O)]^{2+}$ + pic.

A recent theoretical study[56] reported a $[^1\mathbf{Ru^{II}}]^{2+}$ complex with a water molecule coordinated to the metal center, while the dpp is constrained to be a tridentate ligand by the rotation of one "forward" ring (i.e., defining the N−Ru−N bite angle) of the dpp ligand away from the metal center. The authors concluded that the hydrogen bonding between the water and the detached N of the dpp ligand leads to energetically favored O_2 evolution. Our study suggests that such a species with an aqua ligand is not required for a catalytic cycle leading to oxygen evolution. Moreover, we carried out an additional investigation to determine the energetics of $[^1\mathbf{Ru^{II}}(OH_2)]^{2+}$ with the water coordinated to the ruthenium $[^1\mathbf{Ru^{II}}]^{2+}$ and the dpp ligand constrained to remain tridentate. We found such a structure that is indeed stabilized by a hydrogen bond from the water molecule to the detached N atom (Supporting

dx.doi.org/10.1021/ic500709h | Inorg. Chem. 2014, 53, 6904−6913

Information Figure S3). This structure has a higher standard free energy (by 9.43 kcal/mol) relative to $[^1\mathbf{Ru^{II}}]^{2+}$ and a solvent water molecule. Furthermore, the amount of distortion of the $[^1\mathbf{Ru^{II}}]^{2+}$ dpp ligand required to allow coordination of the H_2O most likely leads to a highly activated process. This result and speculation are supported experimentally by there being no change observed in the NMR spectrum of $[^1\mathbf{Ru^{II}}]^{2+}$ dissolved in water over a period of days.

The UV–vis spectrum of $[\mathbf{Ru^{II}}]^{2+}$ in water is typical of a Ru based polypyridine complex with a MLCT band around 540 nm and ligand-based transitions around 330 nm (Figure 2 and

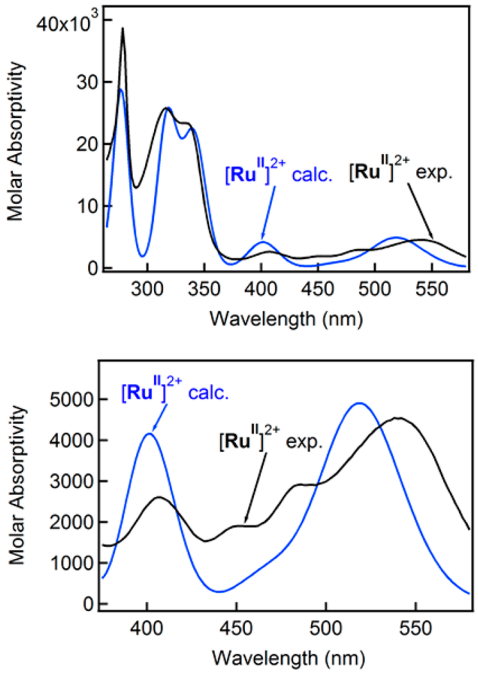

Figure 2. Theoretical (TD-B3LYP; CPCM with UAHF radii) and experimental spectra of $[\mathbf{Ru^{II}}]^{2+}$, where the intensity of the calculated spectra was scaled to the experimental data by a factor of 0.35. The Gaussian peak broadening width is 0.12 eV. The upper and lower spectra show the 290–600 and 375–580 nm ranges, respectively.

Supporting Information Figure S4). The DFT-calculated UV–vis spectrum of $[\mathbf{Ru^{II}}]^{2+}$ matches the experimental spectrum reasonably well (Figure 2); however, a poor match in the spectrum below 375 nm was found for the species resulting from the substitution of a water molecule for one 4-picoline ligand (see Supporting Information Figure S5). The experimental MLCT band for $[^1\mathbf{Ru^{II}}]^{2+}$ appears at 540 nm, and it is predicted by TD-DFT (B3LYP) to be at 519 nm in aqueous solution.

Electrochemistry of $[\mathbf{Ru^{II}}]^{2+}$ in Water: Experimental Results and DFT Analysis. The redox properties of $[\mathbf{Ru^{II}}]^{2+}$ were investigated using cyclic voltammograms (CV) and square wave voltammograms (SWV) in aqueous solutions over the pH range 1–12 (Supporting Information Figures S6–S7) and are summarized in the form of a Pourbaix diagram in Figure 3. DFT calculated redox couples of relevant species are summarized in Table 1 and Scheme 1. Calculated relative free energies of selected species involved in the catalytic cycle with respect to the reference species $[\mathbf{Ru^{II}}]^{2+}$ are presented in Supporting Information Table S1. We have tabulated the potentials of the various couples at pH 0 (the standard state for all potentials and free energies involving a proton) and pH 9

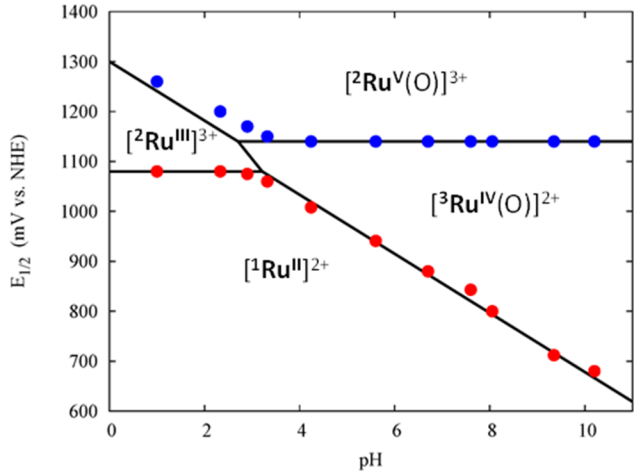

Figure 3. Experimental Pourbaix diagram of $[\mathbf{Ru^{II}}]^{2+}$.

Scheme 1. Possible Sequences of Reactions and Intermediates Involved in the Catalytic Water Oxidation Process by $[^1\mathbf{Ru^{II}}]^{2+}$ with Associated Reduction Potentials at pH 0 and 9

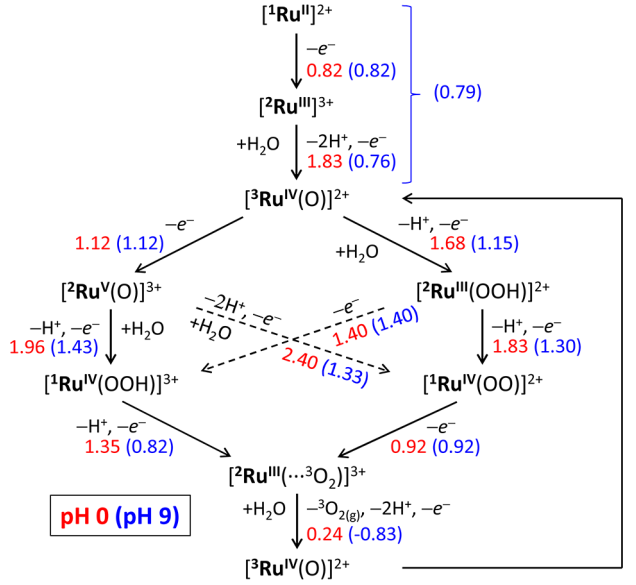

because both the experimental and theoretical results show a marked difference in the electrochemical behavior at low and high pH.

As shown in Figure 3, the topology of the Pourbaix diagram reveals *unique redox chemistry* for this complex compared to other known water oxidation ruthenium(II) complex catalysts. The first oxidation process in the acidic regime between pH 1 and 3 is independent of pH, however as the solution becomes more alkaline (in the pH range 3–8) a change of slope to −59 mV/pH occurs, indicative of a PCET process. We assign the first oxidation event occurring at 1.08 V at low pH to a $[\mathbf{Ru^{III}}]^{2+}/[\mathbf{Ru^{II}}]^{2+}$ couple. DFT calculations show that electron transfer (eq 4) at 0.82 V is energetically favored over the $1e^-/1H^+$ PCET process to $[\mathbf{Ru^{III}}(OH)]^{2+}$ (eq 5) at low pH.

$$[^1\mathbf{Ru^{II}}]^{2+} \rightarrow [^2\mathbf{Ru^{III}}]^{3+} + e^-,\ E^\circ = 0.82\ \text{V (pH 0)} \qquad (4)$$

dx.doi.org/10.1021/ic500709h | Inorg. Chem. 2014, 53, 6904–6913

$$[^{1}\mathbf{Ru}^{\mathbf{II}}]^{2+} + H_2O \rightarrow [^{2}\mathbf{Ru}^{\mathbf{III}}(OH)]^{2+} + e^- + H^+, \quad E^\circ = 1.47\ \text{V (pH 0)} \tag{5}$$

At higher pH (pH > 3), the first-oxidation process is assigned to an energetically favorable $2e^-/2H^+$ PCET reaction of the $[^{1}\mathbf{Ru}^{\mathbf{II}}]^{2+}$ complex and a water molecule to form $[^{3}\mathbf{Ru}^{\mathbf{IV}}(O)]^{2+}$ (eq 6). We confirmed the two-electron nature of the first-oxidation potential by a controlled-potential electrolysis experiment in which a fixed potential of +1050 mV vs NHE (135 mV greater than the first oxidation potential) at pH 6 resulted in a Coulomb count corresponding to a *two-electron* oxidation process. The product of this two-electron oxidation corresponded to the species $[\mathbf{Ru}^{\mathbf{IV}}(O)]^{+}$ as measured by ESI-MS (Supporting Information Figure S8). Calculations show that this step (eq 6) is more energetically favorable at high pH than the stepwise $1e^-/1H^+$ oxidation pathway that leads to a $[\mathbf{Ru}^{\mathbf{III}}(OH)]^{2+}$ species (eq 7) followed by another $1e^-/1H^+$ PCET oxidation to $[\mathbf{Ru}^{\mathbf{IV}}(O)]^{2+}$.

$$[^{1}\mathbf{Ru}^{\mathbf{II}}]^{2+} + H_2O \rightarrow [^{3}\mathbf{Ru}^{\mathbf{IV}}(O)]^{2+} + 2e^- + 2H^+, \quad E^{\circ\prime} = 0.79\ \text{V (pH 9)} \tag{6}$$

$$[^{1}\mathbf{Ru}^{\mathbf{II}}]^{2+} + H_2O \rightarrow [^{2}\mathbf{Ru}^{\mathbf{III}}(OH)]^{2+} + e^- + H^+, \quad E^{\circ\prime} = 0.94\ \text{V (pH 9)} \tag{7}$$

The $[^{2}\mathbf{Ru}^{\mathbf{III}}]^{3+}$ species could, according to the thermodynamics predicted by DFT, react with H_2O via a $1e^-/1H^+$ PCET oxidation to form $[^{1}\mathbf{Ru}^{\mathbf{IV}}(OH)]^{3+}$ at low pH, but our calculations predict this reaction to occur at a higher potential (1.61 V vs NHE) than the $1e^-/2H^+$ PCET oxidation to $[^{3}\mathbf{Ru}^{\mathbf{IV}}(O)]^{2+}$ (eq 8) and the $2e^-/2H^+$ PCET oxidation to $[^{2}\mathbf{Ru}^{\mathbf{V}}(O)]^{3+}$ (eq 9). $[^{3}\mathbf{Ru}^{\mathbf{IV}}(O)]^{2+}$ is experimentally observable and theoretically stable; thus we propose that the next oxidation steps involving $[^{2}\mathbf{Ru}^{\mathbf{III}}]^{3+}$ are the reaction to form $[^{3}\mathbf{Ru}^{\mathbf{IV}}(O)]^{2+}$ (eq 8) and the $2e^-/2H^+$ reaction to from $[^{3}\mathbf{Ru}^{\mathbf{V}}(O)]^{3+}$ (eq 9). We could not, however, experimentally observe the $1e^-/2H^+$ PCET couple between $[\mathbf{Ru}^{\mathbf{III}}]^{3+}$ and a water molecule to form $[\mathbf{Ru}^{\mathbf{IV}}(O)]^{2+}$ between pH 1 and 4 (even with the slow scan rate of 5 mV/s) and by using different combinations of working electrodes (for example, FTO and boron-doped diamond) because of the small peak to peak separation (ΔE = 20 mV). This process may also have sluggish kinetics on the time scale of the electrochemistry measurements.

$$[^{2}\mathbf{Ru}^{\mathbf{III}}]^{3+} + H_2O \rightarrow [^{3}\mathbf{Ru}^{\mathbf{IV}}(O)]^{2+} + e^- + 2H^+, \ E^\circ = 1.83\ \text{V (pH 0)};\ E^{\circ\prime} = 0.76\ \text{V (pH 9)} \tag{8}$$

$$[^{2}\mathbf{Ru}^{\mathbf{III}}]^{3+} + H_2O \rightarrow [^{2}\mathbf{Ru}^{\mathbf{V}}(O)]^{2+} + 2e^- + 2H^+, \quad E^\circ = 1.47\ \text{V (pH 0)};\ E^{\circ\prime} = 0.94\ \text{V (pH 9)} \tag{9}$$

The reaction in eq 8 is followed by the $1e^-$ oxidation of $[^{3}\mathbf{Ru}^{\mathbf{IV}}(O)]^{2+}$ at 1120 mV to $[^{2}\mathbf{Ru}^{\mathbf{V}}(O)]^{3+}$ (eq 10). Experimentally, this second oxidation event at pH > 4 is observed as a pH-independent one-electron oxidation process. This ET process occurs at relatively low potential in comparison with other known ruthenium(II) polypyridine complexes, particularly six-coordinate complexes that already contain water as a sixth coordinating *axial* ligand in their coordination sphere,[31,57−60] for example, the $[\mathbf{Ru}^{\mathbf{V}}(O)]^{3+}/\mathbf{Ru}^{\mathbf{IV}}(O)]^{2+}$ couple of Ru(tpy)(bpm)$(OH_2)]^{2+}$ is at 1.6 V vs NHE.[58] Related ruthenium(II) complexes with a sixth *equatorial* aqua ligand have lower $[\mathbf{Ru}^{\mathbf{V}}(O)]^{3+}/\mathbf{Ru}^{\mathbf{IV}}(O)]^{2+}$ potentials because of the interaction of the Ru dπ orbitals with the π^* orbital of the equatorial polypyridyl ligand and the p_π orbitals of the O ligand.[18,19] In the present case, we calculate 1.12 V compared to the experimental 1.14 V.

$$[^{3}\mathbf{Ru}^{\mathbf{IV}}(O)]^{2+} \rightarrow [^{2}\mathbf{Ru}^{\mathbf{V}}(O)]^{3+} + e^-, \quad E^\circ = 1.12\ \text{V (pH 0, 9)} \tag{10}$$

To confirm these assignments, we performed bulk electrolysis of $[\mathbf{Ru}^{\mathbf{II}}]^{2+}$ at pH 1 at a fixed potential of +1350 mV (100 mV greater than the second oxidation potential), which yielded a Coulomb count corresponding to a *three-electron* oxidation process consistent with the formation of $[\mathbf{Ru}^{\mathbf{V}}(O)]^{3+}$. However, the ESI-MS of the resulting solution was consistent with the $[\mathbf{Ru}^{\mathbf{IV}}(^{16}O)]^{2+}$ species and was confirmed by producing the isotopically labeled analogue $[\mathbf{Ru}^{\mathbf{IV}}(^{18}O)]^{2+}$ using $H_2{}^{18}O$ as a solvent (Supporting Information Figure S9). It is possible that the redox unstable $[\mathbf{Ru}^{\mathbf{V}}(O)]^{3+}$ species is reduced to $[\mathbf{Ru}^{\mathbf{IV}}(O)]^{2+}$ during sample transfer or the MS acquisition process. Despite this complication, the ESI-MS experiment confirms the existence of a seven-coordinate species in the catalytic mechanism.

Coulometric experiments at pH 6 at a fixed potential of 1400 mV vs NHE (250 mV above the $[\mathbf{Ru}^{\mathbf{V}}(O)]^{3+}/\mathbf{Ru}^{\mathbf{IV}}(O)]^{2+}$) couple resulted in an oxidation process that consumed more than three electrons (3.5 e^- from the Coulomb count). This is probably the result of the applied potential of 1400 mV being very close to the half-potential for the $[^{1}\mathbf{Ru}^{\mathbf{IV}}(OO)]^{2+}/[^{2}\mathbf{Ru}^{\mathbf{V}}(O)]^{3+}$ (or $[^{1}\mathbf{Ru}^{\mathbf{IV}}(OOH)]^{3+}/[^{2}\mathbf{Ru}^{\mathbf{V}}(O)]^{3+}$) couple, depending on the actual pK_a of $[^{1}\mathbf{Ru}^{\mathbf{IV}}(OOH)]^{3+}$, which represents the rate-limiting step in the water oxidation mechanism according to our DFT calculations (vide infra). A contribution to the catalytic current may be responsible for the offset in electron count obtained.

The $[^{2}\mathbf{Ru}^{\mathbf{V}}(O)]^{3+}$ reacts with a water molecule in concert with a $1e^-/H^+$ PCET at low pH or a $1e^-/2H^+$ PCET at high pH to afford a hydroperoxo (eq 11) or peroxo species (eq 12), respectively.

$$[^{2}\mathbf{Ru}^{\mathbf{V}}(O)]^{3+} + H_2O \rightarrow [^{1}\mathbf{Ru}^{\mathbf{IV}}(OOH)]^{3+} + e^- + H^+, \quad E^\circ = 1.96\ \text{V (pH 0)} \tag{11}$$

$$[^{2}\mathbf{Ru}^{\mathbf{V}}(O)]^{3+} + H_2O \rightarrow [^{1}\mathbf{Ru}^{\mathbf{IV}}(OO)]^{2+} + e^- + 2H^+, \quad E^{\circ\prime} = 1.33\ \text{V (pH 9)} \tag{12}$$

Indeed, the addition of 10 equiv of Ce(IV) to $[\mathbf{Ru}^{\mathbf{II}}]^{2+}$ resulted in the rapid consumption of the starting material and the formation of an oxidized species with a UV−vis absorption band around 335 nm. The 335 nm absorbing species disappeared on ∼60 s time scale resulting in the formation of a 360 nm species (Supporting Information Figure S10A). The 360 band decayed gradually, resulting in the formation of a new species which absorbs around 425 nm (Supporting Information Figure S10 B). Interestingly, the induction period in O_2 evolution coincides with the formation kinetics of the 425 nm species, and the onset of catalytic current does not start until a substantial amount of this species is formed (Supporting Information Figure S11) The 360 nm species was assigned as $[\mathbf{Ru}^{\mathbf{V}}(O)]^{3+}$ and the 425 nm species, based on mass spectrometry (m/z = 327), was assigned as $[\mathbf{Ru}^{\mathbf{IV}}(OO)]^{2+}$

dx.doi.org/10.1021/ic500709h | Inorg. Chem. 2014, 53, 6904−6913

formed by the loss of a proton from the expected $[\mathbf{Ru^{V}}(OOH)]^{3+}$, which is within experimental error (Supporting Information Figure S12). It should be noted that the m/z = 327 signal was observed only after the incubation time necessary for the formation of 425 nm band. The resonance Raman spectrum of the solution after the induction period shows a new vibrational band around 830 cm^{-1} not present in the parent $[\mathbf{Ru^{II}}]^{2+}$ spectrum (Supporting Information Figure S13). This vibration shifts ~16 cm^{-1} upon ^{18}O isotopic labeling. Under the conditions of the experiment, the solution would be expected to contain a number of oxidized catalyst species including $[\mathbf{Ru^{IV}}(OOH)]^{3+}$ and $[^{2}\mathbf{Ru^{V}}(O)]^{3+}$. According to our DFT calculations the frequency of the O−O vibration (strongly mixed with ligand vibrations) in the $[\mathbf{Ru^{IV}}(OOH)]^{3+}$ species is at 847.71 cm^{-1}. Our calculations further predict that the formation of $[\mathbf{Ru^{IV}}(OOH)]^{3+}$ at low pH or $[\mathbf{Ru^{IV}}(OO)]^{2+}$ at high pH (eqs 11 and 12) may be one of the slow kinetic steps, consistent with the observed correlation between the formation kinetics of the 425 nm species and the induction period in the evolution of catalytic current. Moreover, the experimental and calculated resonance Raman spectra of $[\mathbf{Ru^{IV}}(OOH)]^{3+}$ agree well (Supporting Information Figure S13).

The option of the $2e^{-}/1H^{+}$ PCET oxidation of $[^{3}\mathbf{Ru^{IV}}(O)]^{2+}$ to $[^{1}\mathbf{Ru^{IV}}(OOH)]^{3+}$ (E^{o} = 1.68 eV) is not energetically favorable compared to eqs 10 and 12, and at high pH it cannot compete with the $2e^{-}/2H^{+}$ PCET oxidation of $[^{3}\mathbf{Ru^{IV}}(O)]^{2+}$ to $[^{1}\mathbf{Ru^{IV}}(OO)]^{2+}$ (eq 13).

$$[^{3}\mathbf{Ru^{IV}}(O)]^{2+} + H_2O \rightarrow [^{1}\mathbf{Ru^{IV}}(OO)]^{2+} + 2e^{-} + 2H^{+}, \quad E^{\circ\prime} = 1.23\ \text{V (pH 9)} \tag{13}$$

$[^{2}\mathbf{Ru^{V}}(O)]^{3+}$ can undergo the addition of water and a concomitant $1e^{-}/1H^{+}$ PCET oxidation to $[^{1}\mathbf{Ru^{IV}}(OOH)]^{3+}$ (eq 14), and this reaction is observed at low pH in the theoretical Pourbaix diagram (Figure 4). $[^{2}\mathbf{Ru^{V}}(O)]^{3+}$ can also undergo a $1e^{-}/2H^{+}$ PCET oxidation to $[^{1}\mathbf{Ru^{IV}}(OO)]^{2+}$ (eq 15) at high pH.

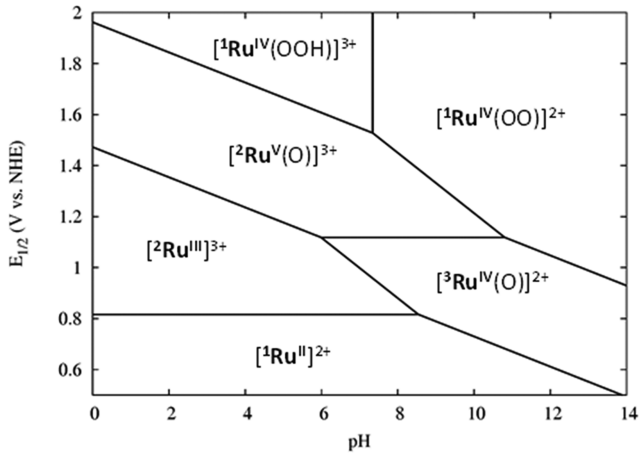

Figure 4. Theoretical Pourbaix diagram of $[\mathbf{Ru^{II}}]^{2+}$. All numerical data are listed in Table 1

$$[^{2}\mathbf{Ru^{V}}(O)]^{3+} + H_2O \rightarrow [^{1}\mathbf{Ru^{IV}}(OOH)]^{3+} + e^{-} + H^{+}, \quad E^{\circ} = 1.96\ \text{V (pH 0)} \tag{14}$$

$$[^{2}\mathbf{Ru^{V}}(O)]^{3+} + H_2O \rightarrow [^{1}\mathbf{Ru^{IV}}(OO)]^{2+} + e^{-} + 2H^{+}, \quad E^{\circ\prime} = 1.33\ \text{V (pH 9)} \tag{15}$$

The $[^{1}\mathbf{Ru^{IV}}(OOH)]^{3+}$ and $[^{1}\mathbf{Ru^{IV}}(OO)]^{2+}$ species are related by the proton transfer reaction corresponding to the pK_a of $[^{1}\mathbf{Ru^{IV}}(OOH)]^{3+}$ (eq 16). At basic pH, the $[^{1}\mathbf{Ru^{IV}}(OO)]^{2+}$ species can undergo a formal one-electron oxidation to make "$[^{2}\mathbf{Ru^{V}}(OO)]^{3+}$" (eq 17), which we found to recouple its spin during geometry optimization to form the weakly bound $[^{2}\mathbf{Ru^{III}}(\cdots{}^{3}O_2)]^{3+}$ complex.

$$[^{1}\mathbf{Ru^{IV}}(OOH)]^{3+} \rightarrow [^{1}\mathbf{Ru^{IV}}(OO)]^{2+} + H^{+}, \quad pK_a = 7.34,\ \Delta G_a^{*} = 0.43\ \text{eV} \tag{16}$$

$$[^{1}\mathbf{Ru^{IV}}(OO)]^{2+} \rightarrow [^{2}\mathbf{Ru^{V}}(OO)]^{3+} + e^{-},\ E^{\circ} = 0.92\ \text{V} \tag{17}$$

There appears to be no place for $[^{2}\mathbf{Ru^{III}}(OOH)]^{2+}$ in the theoretical Pourbaix diagram, and the only important pK_a is that of $[^{1}\mathbf{Ru^{IV}}(OOH)]^{3+}$, its one-electron-oxidized species. Also, there appears to be no place for $[^{2}\mathbf{Ru^{III}}(OH)]^{2+}$, $[^{1}\mathbf{Ru^{IV}}(OH)]^{3+}$, or $[^{1}\mathbf{Ru^{IV}}(O)]^{2+}$ because other species can be formed from their precursors at lower potential. These "discarded" species can at most be involved only transiently under certain conditions. Considering all predicted values of reduction potentials and the pK_a from the DFT calculations (Table 1 and Supporting Information Table S1) a theoretical Pourbaix diagram can be constructed (Figure 4) that is more complete than the experimental one.

The theoretical Pourbaix diagram in Figure 4 is corroborated by several key features of the experimental one (Figure 3), which is less complete because of the difficulty in observing multielectron, multiproton oxidation steps that are slow on the time scale of a cyclic voltamogram (CV) scan (Figure S6). The first oxidation at low pH involves only electron transfer (i.e., the potential is independent of pH), but at higher pH the first oxidation potential has a pH dependence of −59 mV/pH indicative of either a $1e^{-}/1H^{+}$ or a $2e^{-}/2H^{+}$ PCET process. The most obvious assignment of these couples is that at low pH the first couple is $[^{2}\mathbf{Ru^{III}}]^{3+}/[^{1}\mathbf{Ru^{II}}]^{2+}$, and at higher pH it is either $[^{2}\mathbf{Ru^{III}}(OH)]^{2+}/[^{1}\mathbf{Ru^{II}}]^{2+}$ or $[^{3}\mathbf{Ru^{IV}}(O)]^{2+}/[^{1}\mathbf{Ru^{II}}]^{2+}$ with the protons and oxygen atom coming from a solvent water molecule.

The second oxidation is pH dependent with a slope of −59 mV/pH at low pH (indicative of either a $1e^{-}/1H^{+}$ or a $2e^{-}/2H^{+}$ PCET process), and independent of pH at higher pH (indicative of an electron transfer process). The second oxidation at higher pH seems to rule out the first oxidation producing $[^{2}\mathbf{Ru^{III}}(OH)]^{2+}$ because then the second oxidation would presumably be the $1e^{-}/1H^{+}$ PCET oxidation to $[^{3}\mathbf{Ru^{IV}}(O)]^{2+}$ which would be pH dependent. If the first oxidation were to $[^{3}\mathbf{Ru^{IV}}(O)]^{2+}$, then the second oxidation would be to $[^{2}\mathbf{Ru^{V}}(O)]^{3+}$, consistent with the observed independence of pH. This is also consistent with the second oxidation at low pH being the $2e^{-}/2H^{+}$ PCET process to $[^{2}\mathbf{Ru^{V}}(O)]^{3+}$. Not observed in the experimental Pourbaix diagram is evidence of the $[^{3}\mathbf{Ru^{IV}}(O)]^{2+}/[^{2}\mathbf{Ru^{III}}]^{3+}$ couple, which is a $1e^{-}/2H^{+}$ process as shown in the theoretical Pourbaix diagram in Figure 4. Taken all together, our assignment of the redox species shown in the experimental Pourbaix diagram in Figure 3 is clearly in agreement with the topology of the theoretical Pourbaix diagram from the DFT calculations (Figure 4). However, the theoretical diagram is

dx.doi.org/10.1021/ic500709h | Inorg. Chem. 2014, 53, 6904−6913

expanded along both the pH and the potential axis compared to the experimental one.

Latimer–Frost Diagrams for Species Involved in the Catalytic Cycle. Using the standard reduction potentials at pH 0 and adjusted potentials at higher pH, we can also construct a theoretical Latimer–Frost diagram at any pH value. As shown in the theoretical Pourbaix diagram (see Figure 4), the species involved in the oxidation process at pH 0 are $[^{1}\mathbf{Ru}^{II}]^{2+}$, $[^{2}\mathbf{Ru}^{III}]^{3+}$, $[^{2}\mathbf{Ru}^{V}(O)]^{3+}$, and $[^{1}\mathbf{Ru}^{IV}(OOH)]^{3+}$. Whereas at basic pH (e.g., pH 9), the species are $[^{1}\mathbf{Ru}^{II}]^{2+}$, $[^{3}\mathbf{Ru}^{IV}(O)]^{2+}$, $[^{2}\mathbf{Ru}^{V}(O)]^{3+}$, and $[^{1}\mathbf{Ru}^{IV}(OO)]^{2+}$. In addition to species which can be placed on the Pourbaix diagram, the reactions relevant to the O_2 evolution step have to be considered (eqs 18–21).

The $[^{2}\mathbf{Ru}^{V}(OO)]^{3+}$ peroxo complex recouples its spin to become $[^{2}\mathbf{Ru}^{III}(\cdots{}^{3}O_2)]^{3+}$, and the oxygen may spontaneously dissociate to produce $[^{2}\mathbf{Ru}^{III}]^{3+}$ (eq 18). If it cannot do this, or if the dissociation is very slow, the $[^{2}\mathbf{Ru}^{III}(\cdots{}^{3}O_2)]^{3+}$ complex would require another oxidation step to dissociate the O_2 molecule (eq 19). This would produce the 16-electron, six-coordinate $[^{3}\mathbf{Ru}^{IV}]^{4+}$ complex that would be unstable in the aqueous solvent, and would spontaneously bind a water molecule leading to the net oxidation reaction producing $[^{3}\mathbf{Ru}^{IV}(O)]^{2+}$ (eqs 20 and 21).

$$[^{2}\mathbf{Ru}^{III}(\cdots{}^{3}O_2)]^{3+} \rightarrow [^{2}\mathbf{Ru}^{III}]^{3+} + {}^{3}O_2,\ \Delta G^{*} = -1.59\ \text{eV} \quad (18)$$

$$[^{2}\mathbf{Ru}^{III}(\cdots{}^{3}O_2)]^{3+} \rightarrow [^{3}\mathbf{Ru}^{IV}]^{4+} + {}^{3}O_2 + e^{-},\ E^{\circ} = 1.04\ \text{V (pH 0)} \quad (19)$$

$$[^{2}\mathbf{Ru}^{III}(\cdots{}^{3}O_2)]^{3+} + H_2O \rightarrow [^{3}\mathbf{Ru}^{IV}(O)]^{2+} + {}^{3}O_2 + e^{-} + 2H^{+},\ E^{\circ} = 0.24\ \text{V (pH 0)} \quad (20)$$

$$[^{2}\mathbf{Ru}^{III}(\cdots{}^{3}O_2)]^{3+} + H_2O \rightarrow [^{3}\mathbf{Ru}^{IV}(O)]^{2+} + {}^{3}O_2 + e^{-} + 2H^{+},\ E^{\circ\prime} = -0.83\ \text{V (pH 9)} \quad (21)$$

The Latimer–Frost diagrams in Figure 5 show the cumulative free-energy change as a function of the number of electrons removed in the oxidation process at pH 0 (lower panel) and pH 9 (upper panel). The dotted lines correspond to the net free-energy change of the 4-electron water oxidation process, and, because the catalyst species is the same at the beginning and end of the 4-electron water oxidation cycle, represent the free-energy change in the reservoir that is the same for any catalyst. The dotted lines represent the thermodynamic limit of the potential required to oxidize water to oxygen, and its slope is calculated here to be 1.17 V/e^{-} at pH 0 (using our calculated or adopted values of the free energies of the reservoir species and our calculated value of the NHE; the experimental value is 1.23 V/e^{-}). This slope is pH dependent when referenced to the NHE, but is independent of pH when referenced to the reversible hydrogen electrode (RHE). The catalyst intermediate lying furthest above this line on a per electron basis will give rise to a thermodynamic contribution to the overpotential associated with the catalyst.

The dotted line drawn in the pH 0 Latimer–Frost diagram (Figure 5) is between the hypothetical 5-electron oxidized species in which the intermediate $[^{2}\mathbf{Ru}^{III}(\cdots{}^{3}O_2)]^{3+}$ spontaneously dissociates the $^{3}O_2$ molecule (blue point), and the resulting 6-coordinate $[^{2}\mathbf{Ru}^{III}]$ reenters the catalytic cycle at the one-electron oxidized point. Indeed, as indicated by the position of the blue point, this is an exothermic reaction (by

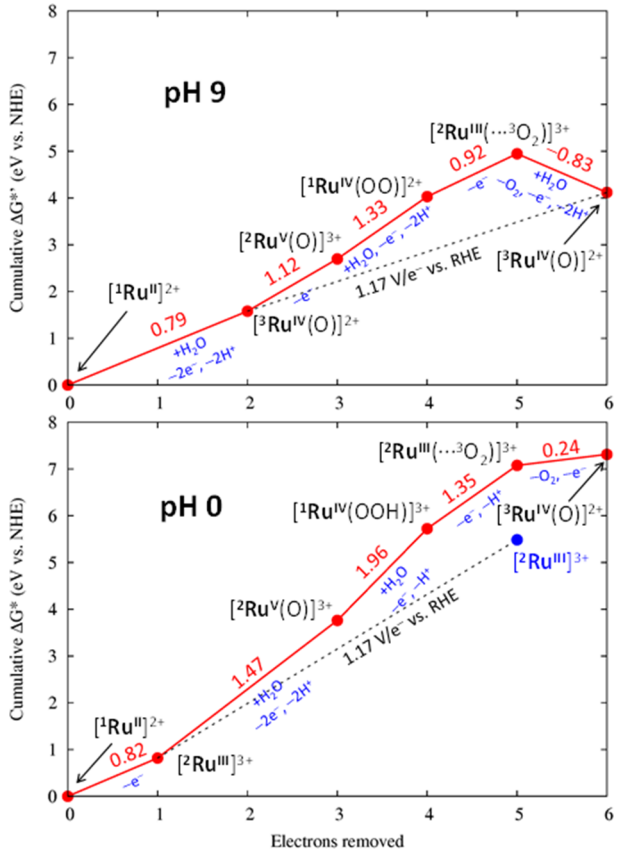

Figure 5. Theoretical Latimer–Frost diagram at pH 0 (lower panel) and pH 9 (upper panel) for the catalytic reaction with $[^{1}\mathbf{Ru}^{II}]^{2+}$. The blue point in the pH 0 diagram indicates the hypothetical intermediate in which the $[^{2}\mathbf{Ru}^{III}(\cdots{}^{3}O_2)]^{3+}$ spontaneously liberates the $^{3}O_2$ molecule and generates the 6-coordinate $[^{2}\mathbf{Ru}^{III}]^{3+}$. All numerical data are presented in Table 1

1.59 eV in our calculations), but it may be sufficiently slow to require an additional oxidation to release the $^{3}O_2$. If an additional oxidation is required, the resulting $[^{3}\mathbf{Ru}^{IV}]^{4+}$ species, as mentioned above, would likely react with a molecule of the solvent water and reenter the catalytic cycle as the seven-coordinate, two-electron-oxidized species $[^{3}\mathbf{Ru}^{IV}(O)]^{2+}$. In the pH 9 Latimer–Frost diagram, the $[^{2}\mathbf{Ru}^{III}(\cdots{}^{3}O_2)]^{3+}$ intermediate is oxidized by the removal of a sixth electron to liberate $^{3}O_2$ and generate the 7-coordinate $[^{3}\mathbf{Ru}^{IV}(O)]^{2+}$ complex (in a pH region in which that species is thermodynamically stable) that reenters the catalytic cycle at the two-electron oxidized point. For pH higher than the pK_a of $[^{1}\mathbf{Ru}^{IV}(OOH)]^{3+}$, after one pass through the catalytic cycle all catalyst species remain seven-coordinate. If $^{3}O_2$ is not liberated by the fifth oxidation, the first pass through the catalytic cycle generates 6 electrons and 6 protons regardless of pH, but above pH ~8.5, subsequent cycles generate only 4 electrons and 4 protons. The dotted line in the pH 0 Latimer–Frost diagram is drawn from the reentry point to the hypothetical dissociated state because that is the only way $^{3}O_2$ evolution at that pH can be achieved by liberating 4 electrons and four protons.

It is clear by comparison of the two Latimer–Frost diagrams in Figure 5 that the one at pH 9 offers the lower energy pathway for water oxidation. The final two steps at pH 9 in principle could be combined into a single $2e^{-}/2H^{+}$ PCET step because the $[^{2}\mathbf{Ru}^{III}(\cdots{}^{3}O_2)]^{3+}$ intermediate lies above the line joining the intermediates before and after it in the reaction

dx.doi.org/10.1021/ic500709h | Inorg. Chem. 2014, 53, 6904–6913

sequence (indicating that $[^2\mathbf{Ru}^{III}(\cdots{}^3O_2)]^{3+}$ is unstable with respect to disproportionation). The step $[^2\mathbf{Ru}^{V}(O)]^{3+} + H_2O \rightarrow [^1\mathbf{Ru}^{IV}(OOH)]^{3+} + H^+ + e^-$ in the pH 0 Latimer-Frost diagram requiring a calculated standard potential of 1.96 V vs NHE is consistent with the experimental observation of an induction period in the kinetics of oxygen evolution using Ce(IV) as a sacrificial oxidant at pH 1 (Supporting Information Figure S14). The underpotential-driven catalytic reaction would eventually reach a steady state that is sustained thereafter.

Once the catalyst enters the catalytic cycle, all rate limiting reactions are PCET transformations at high pH, however the most energetically demanding step at low pH is not helped much by its PCET nature. This is evident from the plot of catalytic onset potentials as a function of pH (Figure S15). At low pH the catalytic onset shows no pH dependence, however above pH 4 a −59 mV/pH dependence is observed.

DISCUSSION

Species Involved in the Catalytic Cycle. A tentative mechanism for the water oxidation process using $[^1\mathbf{Ru}^{II}]^{2+}$ was proposed by Thummel and co-workers.[32] To confirm some aspects of the coordination number and the energetics of the studied system, preliminary DFT calculations were performed. It was shown that the starting species $[^1\mathbf{Ru}^{II}]^{2+}$ is a six-coordinate complex. The addition of an H_2O molecule to the metal center in the equatorial position leads to the dissociation of this ligand during the optimization of the $[^1\mathbf{Ru}^{II}(OH_2)]^{2+}$ and $[^2\mathbf{Ru}^{III}(OH_2)]^{2+}$ species, but not for the $[^3\mathbf{Ru}^{IV}(OH_2)]^{4+}$ species (the triplet complex is more stable than the corresponding singlet complex by ∼10 kcal/mol), which can undergo two PCET oxidations and become the pentagonal bipyrimidal $[^3\mathbf{Ru}^{IV}(O)]^{2+}$ (more stable than the corresponding singlet complex by ca. 6 kcal/mol). Those calculations also identified a stable $[^3\mathbf{Ru}^{IV}(OOH)]^{3+}$ species. The tentatively proposed catalytic scheme in that work was initiated by the two-electron oxidation of the 18-electron, six-coordinate $[^1\mathbf{Ru}^{II}]^{2+}$ complex to produce the 16-electron $[^3\mathbf{Ru}^{IV}]^{4+}$ species, which incorporated a molecule of the solvent water to have an 18-electron metal center.

In the present study, we found that the "19-electron" $[^2\mathbf{Ru}^{III}(OH)]^{2+}$ has a bound hydroxide ion in an equatorial position, but the resulting complex is relatively high in energy and has a partially detached (i.e., tridentate) dpp ligand. However, we found a bound structure and a reasonable energy for the 19-electron $[^2\mathbf{Ru}^{III}(OOH)]^{2+}$ and explored its possible involvement in the catalytic cycle despite its also having a partially detached dpp ligand. While the singlet states of $[^1\mathbf{Ru}^{IV}(OH_2)]^{4+}$ and $[^1\mathbf{Ru}^{IV}(OH)]^{3+}$ (Supporting Information Figure S16) appear to be more stable than the corresponding triplets, the triplet state $[^3\mathbf{Ru}^{IV}(O)]^{2+}$ has lower energy (by 6.69 kcal/mol) than $[^1\mathbf{Ru}^{IV}(O)]^{2+}$. The singlet states of these species all have 18-electron metal centers, so this suggests that $[^3\mathbf{Ru}^{IV}(O)]^{2+}$ has significant $[^2\mathbf{Ru}^{III}(O^{\bullet-})]^{2+}$ character to accommodate two unpaired electrons. In fact, Supporting Information Figure S17 shows that the two unpaired electrons reside in different π^* orbitals associated with the Ru−O bond. Further consideration of $[^3\mathbf{Ru}^{IV}(O)]^{2+}$ as a key intermediate in catalytic water oxidation was therefore appropriate. Because $[^3\mathbf{Ru}^{IV}(O)]^{2+}$ has the lower energy, there is no pK_a that can be associated with $[^1\mathbf{Ru}^{IV}(OH)]^{3+}$ (Supporting Information Figure S16) in a Pourbaix diagram. However, we were able to calculate the pK_a of the $[^1\mathbf{Ru}^{IV}(OOH)]^{3+}$ that produces $[^1\mathbf{Ru}^{IV}(OO)]^{2+}$, both of which were predicted to be key species in the catalytic cycle (see Scheme 1).

There is a very small difference in energy (0.40 kcal/mol) between the two species that might formally be labeled $[^2\mathbf{Ru}^{V}(OO)]^{3+}$ and $[^4\mathbf{Ru}^{V}(OO)]^{3+}$ with the $[^4\mathbf{Ru}^{V}(OO)]^{3+}$ complex having the lower energy. There is spin recoupling in the nominal $[\mathbf{Ru}^{V}(OO)]^{3+}$ complexes from a doublet or quartet metal center and a peroxide dianion to a doublet metal center and a loosely bound $^3O_2$ molecule in the final optimized $[\mathbf{Ru}^{III}(\cdots{}^3O_2)]^{3+}$ complexes. We assign it here as a doublet because it is formed by the one-electron PCET oxidation of $[^1\mathbf{Ru}^{IV}(OOH)]^{3+}$ or the one-electron oxidation of $[^1\mathbf{Ru}^{IV}(OO)]^{2+}$, the aforementioned key species. During the optimization of both doublet and quartet states, the O−O ligand moves away from the metal center to a distance of ∼5 Å to the nearer O atom (Supporting Information Figure S18). Actually removing the oxygen molecule from $[^2\mathbf{Ru}^{III}(\cdots{}^3O_2)]^{3+}$ is overall an exothermic reaction, however, because the quartet state, which should be able to dissociate directly to doublet and triplet states, does not completely dissociate the $^3O_2$ molecule, this process is likely to be activated and kinetically slow. The calculation of the $[^{1,3}\mathbf{Ru}^{VI}(O)]^{4+}$ species indicates that the triplet state is more stable by 7.46 kcal/mol, however, we now believe that $\mathbf{Ru}^{VI}$ and its derivative species have little probability of being involved in the catalysis owing to their relatively high energy. The four electrons and four protons required in the water oxidation process can be obtained during the catalysis without reaching an oxidation state as high as the $\mathbf{Ru}^{VI}$ state.

As mentioned above, in some species (e.g., $[^2\mathbf{Ru}^{III}(OOH)]^{2+}$, $[^2\mathbf{Ru}^{III}(OH)]^{2+}$ and $[^3\mathbf{Ru}^{IV}(OH)]^{3+}$) the tetradentate dpp ligand loses its four-coordinate property, and becomes a tridentate ligand through detachment of one of the "front" Ru−N(dpp) bonds (i.e., defining the wide bite angle of the ligand). This is not surprising in view of the fact that they are all formally 19-electron systems with a seventh coordinating ligand that cannot accommodate extra negative charge. The detailed structures and other molecular properties of all analyzed species are listed in the Supporting Information (Figures S19−S21 and Tables S2−S4).

Possible Reaction Pathways. On the basis of the energetics of the calculated species, we examined possible reaction mechanisms (see Figure 5) involving two pathways depending on the pH of the solution. The low pH pathway goes from $[^1\mathbf{Ru}^{II}]^{2+}$ through $[^2\mathbf{Ru}^{III}]^{3+}$ and $[^2\mathbf{Ru}^{V}(O)]^{3+}$ to $[^1\mathbf{Ru}^{IV}(OOH)]^{3+}$ to obtain $[^2\mathbf{Ru}^{III}(\cdots{}^3O_2)]^{2+}$ (which starts out as $[^2\mathbf{Ru}^{V}(OO)]^{3+}$ and nearly dissociates $^3O_2$ during optimization), and the high pH pathway goes through $[^3\mathbf{Ru}^{IV}(O)]^{2+}$ and $[^2\mathbf{Ru}^{V}(OO)]^{3+}$ to $[^1\mathbf{Ru}^{IV}(OO)]^{2+}$ to reach the same point of $[^2\mathbf{Ru}^{III}(\cdots{}^3O_2)]^{3+}$.

The thermodynamics of the various possible pathways were predicted theoretically, and it was found, for example, that the PCET process from $[^3\mathbf{Ru}^{IV}(O)]^{2+}$ to $[^2\mathbf{Ru}^{III}(OOH)]^{2+}$ requires a higher potential (1.68 V) than an electron transfer from $[^3\mathbf{Ru}^{IV}(O)]^{2+}$ to $[^2\mathbf{Ru}^{V}(O)]^{3+}$ (1.12 eV, eq 10). With so many possible reactions, the principal difficulty in elucidating the catalytic water oxidation mechanism was to determine which species should appear in the Pourbaix diagram, and appropriately matching them to neighboring species. Consistent with our calculations and our experimental findings, it appears that at high pH the catalytic pathway begins with a PCET process from $[^1\mathbf{Ru}^{II}]^{2+}$ to $[^3\mathbf{Ru}^{IV}(O)]^{2+}$ involving the transfer of two electrons and two protons.

dx.doi.org/10.1021/ic500709h | Inorg. Chem. 2014, 53, 6904−6913

To complete the catalytic cycle at low pH, it might be necessary to further oxidize the $[^{2}\mathbf{Ru}^{III}(\cdots{}^{3}O_2)]^{3+}$ species to create the six-electron-oxidized $[^{3}\mathbf{Ru}^{IV}]^{4+}$ complex and molecular oxygen. As proposed in ref 32, the 16-electron metal center in $[^{3}\mathbf{Ru}^{IV}]^{4+}$ is likely to bind a solvent water molecule as an equatorial ligand in a seven-coordinate complex. In the present work, this is envisioned to be accompanied by the loss of the two protons upon coordinating a water molecule, even if the $[^{3}\mathbf{Ru}^{IV}(O)]^{4+}$ species is not thermodynamically stable at low pH. This would allow the prevailing mechanisms at both low and high pH to reenter the catalytic cycle with a seven-coordinate species, and remain seven-coordinate thereafter. If the $[^{2}\mathbf{Ru}^{III}(\cdots{}^{3}O_2)]^{3+}$ species spontaneously dissociates the loosely bound oxygen molecule, the resulting $[^{2}\mathbf{Ru}^{III}]^{3+}$ complex would reenter the catalytic cycle as the six-coordinate, one-electron-oxidized species at low pH.

CONCLUSIONS

Through a combination of DFT calculations and experimental measurements, we have elucidated the key intermediates in the water oxidation mechanism of the $[Ru(dpp)(pic)_2]^{2+}$ catalyst, which has no aqua ligand in its primary coordination shell. Our results indicate that the first or second step of the mechanism, depending on the pH, involves a seven-coordinate intermediate and that the remaining steps in the first cycle, and likely all steps in subsequent cycles, proceed through an unprecedented sequence of seven-coordinate intermediates. This mechanism reveals an entirely "new chemistry" for water oxidation by polypyridyl ruthenium complexes of this type.

ASSOCIATED CONTENT

Supporting Information

Figures showing ESI/MS of $[\mathbf{Ru}^{II}]^{2+}$, ^{1}H spectra of 4-picoline and $[\mathbf{Ru}^{II}(OH_2)]^{2+}$, UV−vis spectra of $[\mathbf{Ru}^{II}]^{2+}$, $[Ru^{II}(dpp)(pic)(OH_2)]^{2+}$, and $[\mathbf{Ru}^{II}(OH_2)]^{2+}$, CV of $[\mathbf{Ru}^{II}]^{2+}$, slow SWV scans of $[\mathbf{Ru}^{II}]^{2+}$, kinetics of O_2 evolution, Raman spectra, O_2 evolution plots, cyclic voltammograms of $[\mathbf{Ru}^{II}]^{2+}$, calcuated structures of $[^{1,3}\mathbf{Ru}^{IV}(OH)]^{3+}$, frontier molecular orbitals of $[^{3,1}\mathbf{Ru}^{IV}(O)]^{2+}$, input geometry of $[^{2,4}\mathbf{Ru}^{V}(\eta^1\text{-}O_2)]^{3+}$, X-ray structure of the dpp ligand and metal center, geometry of optimized species, calculated free energies, selected bond lengths and angles, species involved in the catalytic cycle, cartesian coordinates of key intermediates, and a geometry discussion. This material is available free of charge via the Internet at http://pubs.acs.org.

AUTHOR INFORMATION

Corresponding Authors

*E-mail: muckerma@bnl.gov.
*E-mail: martak@bnl.gov.

Notes

The authors declare no competing financial interest.

ACKNOWLEDGMENTS

The work at Brookhaven National Laboratory (BNL) was carried out under contract DE-AC02-98CH10886 and the work at Houston was carried out under contract DE-FG02-07ER15888 with the U.S. Department of Energy and supported by its Division of Chemical Sciences, Geosciences, & Biosciences, Office of Basic Energy Sciences. We thank Liu Yang for carrying out some of the DFT calculations. This research utilized computing resources at the Center for Functional Nanomaterials at Brookhaven National Laboratory.

REFERENCES

(1) Lewis, N. S.; Nocera, D. G. *Proc. Natl. Acad. Sci. U.S.A.* **2006**, *103*, 15729−15735.
(2) Kanan, M. W.; Nocera, D. G. *Science* **2008**, *321*, 1072−1075.
(3) Concepcion, J. J.; Jurss, J. W.; Brennaman, M. K.; Hoertz, P. G.; Patrocinio, A. O. T.; Iha, N. Y. M.; Templeton, J. L.; Meyer, T. J. *Acc. Chem. Res.* **2009**, *42*, 1954−1965.
(4) Liu, X.; Wang, F. Y. *Coord. Chem. Rev.* **2012**, *256*, 1115−1136.
(5) Cao, R.; Lai, W. Z.; Du, P. W. *Energy Environ. Sci.* **2012**, *5*, 8134−8157.
(6) Wasylenko, D. J.; Palmer, R. D.; Berlinguette, C. P. *Chem. Commun.* **2013**, *49*, 218−227.
(7) McEvoy, J. P.; Brudvig, G. W. *Chem. Rev.* **2006**, *106*, 4455−4483.
(8) Meyer, T. J.; Huynh, M. H.; Thorp, H. H. *Angew. Chem., Int. Ed.* **2007**, *46*, 5284−5304.
(9) Huynh, M. H.; Meyer, T. J. *Chem. Rev.* **2007**, *107*, 5004−5064.
(10) Umena, Y.; Kawakami, K.; Shen, J. R.; Kamiya, N. *Nature* **2011**, *473*, 55−60.
(11) Weinberg, D. R.; Gagliardi, C. J.; Hull, J. F.; Murphy, C. F.; Kent, C. A.; Westlake, B. C.; Paul, A.; Ess, D. H.; McCafferty, D. G.; Meyer, T. J. *Chem. Rev.* **2012**, *112*, 4016−4093.
(12) Gagliardi, C. J.; Vannucci, A. K.; Concepcion, J. J.; Chen, Z. F.; Meyer, T. J. *Energy Environ. Sci.* **2012**, *5*, 7704−7717.
(13) Nyhlen, J.; Duan, L. L.; Akermark, B.; Sun, L. C.; Privalov, T. *Angew. Chem., Int. Ed.* **2010**, *49*, 1773−1777.
(14) Tong, L. P.; Duan, L. L.; Xu, Y. H.; Privalov, T.; Sun, L. C. *Angew. Chem., Int. Ed.* **2011**, *50*, 445−449.
(15) Duan, L.; Bozoglian, F.; Mandal, S.; Stewart, B.; Privalov, T.; Llobet, A.; Sun, L. *Nat. Chem.* **2012**, *4*, 418−423.
(16) Hirahara, M.; Ertem, M. Z.; Komi, M.; Yamazaki, H.; Cramer, C. J.; Yagi, M. *Inorg. Chem.* **2013**, *52*, 6354−6364.
(17) Piccinin, S.; Sartorel, A.; Aquilanti, G.; Goldoni, A.; Bonchio, M.; Fabris, S. *Proc. Natl. Acad. Sci. U.S.A.* **2013**, *110*, 4917−4922.
(18) Polyansky, D. E.; Muckerman, J. T.; Rochford, J.; Zong, R.; Thummel, R.; Fujita, E. *J. Am. Chem. Soc.* **2011**, *133*, 14649−14665.
(19) Badiei, Y. M.; Polyansky, D. E.; Muckerman, J. T.; Szalda, D. J.; Haberdar, R.; Zong, R.; Thummel, R. P.; Fujita, E. *Inorg. Chem.* **2013**, *52*, 8845−8850.
(20) Kimoto, A.; Yamauchi, K.; Yoshida, M.; Masaoka, S.; Sakai, K. *Chem. Commun.* **2012**, *48*, 239−241.
(21) Bozoglian, F.; Romain, S.; Ertem, M. Z.; Todorova, T. K.; Sens, C.; Mola, J.; Rodriguez, M.; Romero, I.; Benet-Buchholz, J.; Fontrodona, X.; Cramer, C. J.; Gagliardi, L.; Llobet, A. *J. Am. Chem. Soc.* **2009**, *131*, 15176−15187.
(22) Bianco, R.; Hay, P. J.; Hynes, J. T. *J. Phys. Chem. A* **2011**, *115*, 8003−8016.
(23) Hughes, T. F.; Friesner, R. A. *J. Phys. Chem. B* **2011**, *115*, 9280−9289.
(24) Lin, X. S.; Hu, X. Q.; Concepcion, J. J.; Chen, Z. F.; Liu, S. B.; Meyer, T. J.; Yang, W. T. *Proc. Natl. Acad. Sci. U.S.A.* **2012**, *109*, 15669−15672.
(25) Marenich, A. V.; Majumdar, A.; Lenz, M.; Cramer, C. J.; Truhlar, D. G. *Angew. Chem., Int. Ed.* **2012**, *51*, 12810−12814.
(26) Vigara, L.; Ertem, M. Z.; Planas, N.; Bozoglian, F.; Leidel, N.; Dau, H.; Haumann, M.; Gagliardi, L.; Cramer, C. J.; Llobet, A. *Chem. Sci.* **2012**, *3*, 2576−2586.
(27) Wang, L.; Duan, L. L.; Stewart, B.; Pu, M. P.; Liu, J. H.; Privalov, T.; Sun, L. C. *J. Am. Chem. Soc.* **2012**, *134*, 18868−18880.
(28) Ghosh, S.; Baik, M. H. *Angew. Chem., Int. Ed.* **2012**, *51*, 1221−1224.
(29) Jarvis, E. A. A.; Lee, B.; Neddenriep, B.; Shoemaker, W. *Chem. Phys.* **2013**, *417*, 8−16.
(30) Staehle, R.; Tong, L. P.; Wang, L.; Duan, L. L.; Fischer, A.; Ahlquist, M. S. G.; Sun, L. C.; Rau, S. *Inorg. Chem.* **2014**, *53*, 1307−1319.

(31) Concepcion, J. J.; Tsai, M. K.; Muckerman, J. T.; Meyer, T. J. *J. Am. Chem. Soc.* **2010**, *132*, 1545−1557.
(32) Tseng, H.-W.; Zong, R.; Muckerman, J. T.; Thummel, R. *Inorg. Chem.* **2008**, *47*, 11763−11773.
(33) Zong, R.; Thummel, R. P *J. Am. Chem. Soc* **2004**, *126*, 10800−10801.
(34) Duan, L. L.; Fischer, A.; Xu, Y. H.; Sun, L. C. *J. Am. Chem. Soc.* **2009**, *131*, 10397−10399.
(35) Becke, A. D. *Phys. Rev. A* **1988**, *38*, 3098−3100.
(36) Lee, C. T.; Yang, W. T.; Parr, R. G. *Phys. Rev. B* **1988**, *37*, 785−789.
(37) Vosko, S. H.; Wilk, L.; Nusair, M. *Can. J. Phys.* **1980**, *58*, 1200−1211.
(38) Becke, A. D. *J. Chem. Phys.* **1993**, *98*, 5648−5652.
(39) Andrae, D.; Haeussermann, U.; Dolg, M.; Stoll, H.; Preuss, H. *Theor. Chem. Acc.* **1990**, *77*, 123−141.
(40) Martin, J. M. L.; Sundermann, A. *J. Chem. Phys.* **2001**, *114*, 3408−3420.
(41) Ditchfield, R.; Hehre, W. J.; Pople, J. A. *J. Chem. Phys.* **1971**, *54*, 724.
(42) Hehre, W. J.; Ditchfield, R.; Pople, J. A. *J. Chem. Phys.* **1972**, *56*, 2257−2261.
(43) Hariharan, P. C.; Pople, J. A. *Theor. Chem. Acc.* **1973**, *28*, 213−222.
(44) Hariharan, P. C.; Pople, J. A. *Mol. Phys.* **1974**, *27*, 209−214.
(45) Gordon, M. S. *Chem. Phys. Lett.* **1980**, *76*, 163−168.
(46) Francl, M. M.; Pietro, W. J.; Hehre, W. J.; Binkley, J. S.; DeFrees, D. J.; Pople, J. A.; Gordon, M. S. *J. Chem. Phys.* **1982**, *77*, 3654−3665.
(47) Barone, V.; Cossi, M. *J. Phys. Chem. A* **1998**, *102*, 1995−2001.
(48) Cossi, M.; Rega, N.; Scalmani, G.; Barone, V. *J. Comput. Chem.* **2003**, *24*, 669−681.
(49) Klamt, A.; Schüürmann, G. *J. Chem. Soc., Perkin Trans. 2* **1993**, 799−805.
(50) Frisch, M. J.; Trucks, G. W.; Schlegel, H. B.; Scuseria, G. E.; Robb, M. A.; Cheeseman, J. R.; Scalmani, G.; Barone, V.; Mennucci, B.; Petersson, G. A.; Nakatsuji, H.; Caricato, M.; Li, X.; Hratchian, H. P.; Izmaylov, A. F.; Bloino, J.; Zheng, G.; Sonnenberg, J. L.; Hada, M.; Ehara, M.; Toyota, K.; Fukuda, R.; Hasegawa, J.; Ishida, M.; Nakajima, T.; Honda, Y.; Kitao, O.; Nakai, H.; Vreven, T.; Montgomery, J. A. J.; Peralta, J. E.; Ogliaro, F.; Bearpark, M.; Heyd, J. J.; Brothers, E.; Kudin, K. N.; Staroverov, V. N.; Keith, T.; Kobayashi, R.; Normand, J.; Raghavachari, K.; Rendell, A.; Burant, J. C.; Iyengar, S. S.; Tomasi, J.; Cossi, M.; Rega, N.; Millam, J. M.; Klene, M.; Knox, J. E.; Cross, J. B.; Bakken, V.; Adamo, C.; Jaramillo, J.; Gomperts, R.; Stratmann, R. E.; Yazyev, O.; Austin, A. J.; Cammi, R.; Pomelli, C.; Ochterski, J. W.; Martin, R. L.; Morokuma, K.; Zakrzewski, V. G.; Voth, G. A.; Salvador, P.; Dannenberg, J. J.; Dapprich, S.; Daniels, A. D.; Farkas, O.; Foresman, J. B.; Ortiz, J. V.; Cioslowski, J.; Fox, D. J. *Gaussian 09*, revision D.01; Gaussian, Inc.: Wallingford, CT, 2013.
(51) Barone, V.; Cossi, M.; Tomasi, J. *J. Chem. Phys.* **1997**, *107*, 3210−3221.
(52) Kelly, C. P.; Cramer, C. J.; Truhlar, D. G. *J. Phys. Chem. B* **2006**, *110*, 16066−16081.
(53) Tissandier, M. D.; Cowen, K. A.; Feng, W. Y.; Gundlach, E.; Cohen, M. J.; Earhart, A. D.; Coe, J. V. *J. Phys. Chem. A* **1998**, *102*, 7787−7794.
(54) Bartmess, J. E. *J. Phys. Chem.* **1994**, *98*, 6420−6424.
(55) Kelly, C. P.; Cramer, C. J.; Truhlar, D. G. *J. Phys. Chem. B* **2007**, *111*, 408−422.
(56) Zhang, G.; Chen, K.; Chen, H.; Yao, J.; Shaik, S. *Inorg. Chem.* **2013**, *52*, 5088−5096.
(57) Takeuchi, K. J.; Thompson, M. S.; Pipes, D. W.; Meyer, T. J. *Inorg. Chem.* **1984**, *23*, 1845−1851.
(58) Concepcion, J. J.; Jurss, J. W.; Templeton, J. L.; Meyer, T. J. *J. Am. Chem. Soc.* **2008**, *130*, 16462−16463.
(59) Chen, Z. F.; Concepcion, J. J.; Hu, X. Q.; Yang, W. T.; Hoertz, P. G.; Meyer, T. J. *Proc. Natl. Acad. Sci. U.S.A.* **2010**, *107*, 7225−7229.
(60) Concepcion, J. J.; Jurss, J. W.; Norris, M. R.; Chen, Z. F.; Templeton, J. L.; Meyer, T. J. *Inorg. Chem.* **2010**, *49*, 1277−1279.